# Video-rate volumetric functional imaging of the brain at synaptic resolution

Rongwen Lu[1], Wenzhi Sun[1], Yajie Liang[1], Aaron Kerlin[1], Jens Bierfeld[2], Johannes D Seelig[1,3], Daniel E Wilson[4], Benjamin Scholl[4], Boaz Mohar[1], Masashi Tanimoto[1,5], Minoru Koyama[1], David Fitzpatrick[4], Michael B Orger[2] & Na Ji[1]

**Neurons and neural networks often extend hundreds of micrometers in three dimensions. Capturing the calcium transients associated with their activity requires volume imaging methods with subsecond temporal resolution. Such speed is a challenge for conventional two-photon laser-scanning microscopy, because it depends on serial focal scanning in 3D and indicators with limited brightness. Here we present an optical module that is easily integrated into standard two-photon laser-scanning microscopes to generate an axially elongated Bessel focus, which when scanned in 2D turns frame rate into volume rate. We demonstrated the power of this approach in enabling discoveries for neurobiology by imaging the calcium dynamics of volumes of neurons and synapses in fruit flies, zebrafish larvae, mice and ferrets *in vivo*. Calcium signals in objects as small as dendritic spines could be resolved at video rates, provided that the samples were sparsely labeled to limit overlap in their axially projected images.**

Understanding neural computation requires the ability to measure how a neuron integrates its multitude of synaptic inputs, as well as how neural ensembles work together during sensory stimulation and motor control. With submicron lateral resolution and optical sectioning ability in scattering brains, two-photon laser-scanning microscopy[1] (2PLSM) has become a powerful tool for monitoring the activity of neurons and their networks *in vivo* through their calcium transients. However, both individual neurons and neural networks may extend over hundreds or even thousands of micrometers in three dimensions. Because conventional 2PLSM images volume by scanning the excitation laser focus serially in 3D, the limited brightness of calcium indicators and the inertia of laser scanning units make it difficult to capture all the calcium transients in a volume at video rate (for example, 30 Hz) while maintaining the ability to resolve synaptic structures such as dendritic spines and axonal boutons.

Considering that for most *in vivo* brain imaging experiments, the positions of neurons as well as their synapses are known and remain unchanged during each imaging session, one does not need to constantly monitor and track their positions in 3D. Instead, we can obtain projected views of 3D volumes via extended depth-of-field imaging[2] by scanning an axially elongated focus (for example, a Bessel beam) in 2D (ref. 3; **Fig. 1a**). For sparsely labeled brain volumes with minimal structural overlap in their 2D projections, we can monitor neural activity at volume rates that are equivalent to the 2D frame rates. Such axially extended Bessel foci have been combined with 2PLSM to image brain slices[4,5]. Using a spatial light modulator to flexibly control the depths of field, we built a module that generated Bessel foci optimized for *in vivo* brain imaging. Easily incorporated into three different 2PLSM systems, this simple module allowed volume-imaging rates of 30 Hz in sparsely labeled samples while maintaining the ability to resolve dendritic spines and axonal boutons. To demonstrate its versatility, we applied the Bessel focus scanning technique to imaging brain volumes of a variety of model systems *in vivo*, such as fruit fly, zebrafish larva, mouse and ferret. High-speed volume imaging was used to measure the tuning properties of dendritic spines in mouse and ferret visual cortices, the synchrony of inhibitory neuron activity in mouse visual cortex, the network dynamics of reticulospinal neurons in the hindbrains of zebrafish larvae and the responses of fruit fly brains to visual stimuli.

## RESULTS

### Optimized Bessel foci enable 30-Hz *in vivo* volume imaging of dendrites, axons and synapses

The volume-imaging module was composed of a phase-only spatial light modulator (SLM) and an annular mask array, and it was incorporated into a 2PLSM by placing it between the excitation laser and the microscope (**Fig. 1b** and **Supplementary Technical Note**). A concentric binary-phase pattern on the SLM generated a ring illumination at the focal plane of lens L1. After spatial filtering with an annular mask, the ring pattern was imaged onto the galvanometer scanners by lenses L2 and L3. This led to an annular illumination on the back pupil plane of the microscope objective and an axially extended focus approximating a Bessel beam. Combining different SLM patterns with distinct annular masks, we generated a series of Bessel foci with various axial full widths at half maximum (axial FWHM, 15 to 400 μm) and numeric apertures (NA, 0.4 to 0.93) (Online Methods
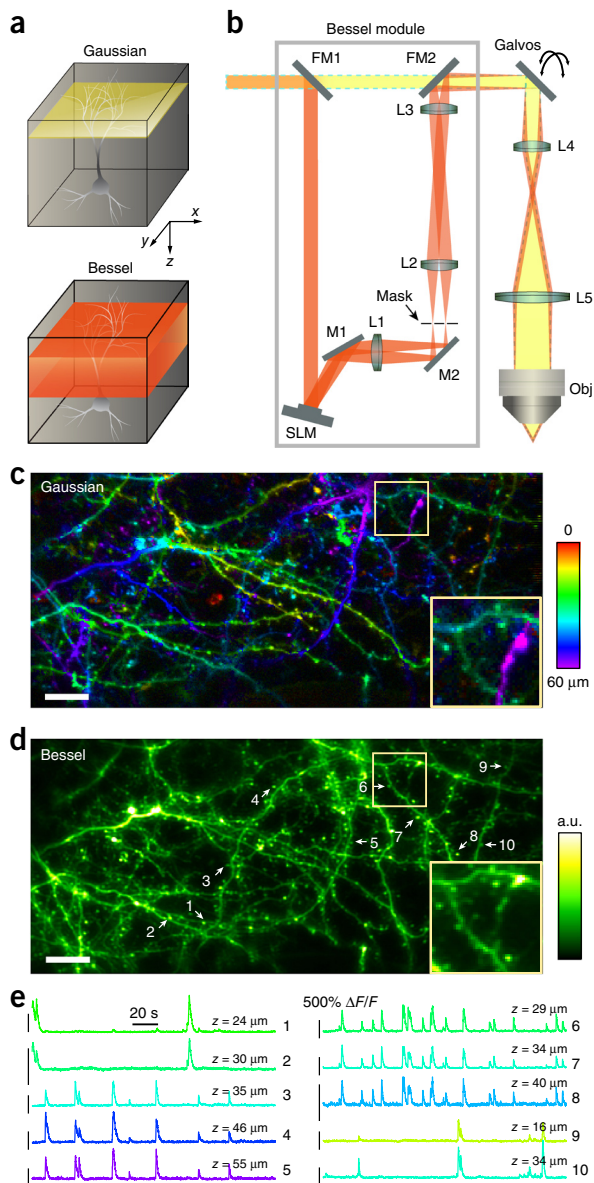
**Figure 1** Concept, design and performance of Bessel module for *in vivo* volume imaging. (**a**) Scanning a Gaussian focus in the *x–y* plane images a thin optical section (yellow-shaded region), whereas scanning a Bessel focus in *x–y* images the structures in a 3D volume (red-shaded region). (**b**) Schematics of Bessel module, composed of an SLM, three lenses (L1, L2, L3) and an annular mask. The module generates an annular illumination pattern on the galvanometers (galvo) and, after conjugation by lenses L4 and L5, at the back pupil of the objective (Obj), resulting in a focus approximating a Bessel beam. M1 and M2, folding mirrors; FM1 and FM2, flip mirrors to switch between Gaussian (yellow with dashed blue outline) and Bessel (red) paths. (**c–e**) Example application of Bessel focus scanning to a volume of GCaMP6s⁺ neurites in awake mouse cortex at 30 Hz. (**c**) Mean intensity projection of a 60-μm-thick image stack collected with Gaussian focus scanning at 1-μm *z* steps, with structures color-coded by depth. (**d**) Image of the same volume of neurites collected by scanning a Bessel focus with 0.4 NA and 53-μm axial FWHM. Arrows and numbers label individual axonal varicosities (putative boutons, 1, 2) and dendritic spines (3–10). Insets in **c** and **d** show zoomed-in views of dendritic spines. Scale bars, 20 μm. (**e**) Representative calcium transients measured in boutons and spines from four neurons (color-coded by *z* depth). Objective, Olympus 25× with 1.05 NA; wavelength, 960 nm; postobjective power, 30 mW for Gaussian and 118 mW for Bessel scanning. Representative images from three mice are shown.

and **Supplementary Technical Note**), and we characterized their performance for *in vivo* brain imaging on three 2PLSM systems (one commercial and two homebuilt systems; see **Supplementary Table 1** for focal lengths of L1–L3 for these systems). We discovered that lower-NA Bessel foci afford better *in vivo* image quality than those with higher NA (**Supplementary Fig. 1**). This is because high-NA Bessel foci have too much energy distributed in their side rings, which, even with suppression by two-photon excitation, still leads to substantial background signal and causes image blur. Because the central peak of a Bessel focus is sharper than that of a Gaussian focus[2], even at NA 0.4 a Bessel focus still has sufficient lateral resolution to resolve individual synaptic terminals but generates much less background haze. Therefore, for all subsequent experiments, we employed Bessel foci with NA 0.4.

To demonstrate the speed and resolution of Bessel volume scanning, we imaged neurites sparsely expressing the genetically encoded calcium sensor GCaMP6s (0–60 μm below pia) in the primary visual cortex (V1) of awake mice. With a Gaussian focus (NA 1.05, axial FWHM 1.4 μm), conventional 3D scanning required a minimum of 36 two-dimensional frames to cover all spines with a volume extending 60 μm in the *z* axis (60 two-dimensional frames were used to generate **Fig. 1c**; and see **Supplementary Table 2**). In contrast, scanning a Bessel focus (NA 0.4, axial FWHM 53 μm; **Fig. 1d**) in 2D captured all the structures in one frame, reducing the data size ~60-fold. Using a 2PLSM with a resonant galvanometer, visually-evoked calcium transients in axonal varicosities and dendritic spines within a 270 μm × 270 μm × 60 μm volume were measured at 30 Hz (**Supplementary Video 1** and **Fig. 1e**). Notably, with Bessel scanning, the gain in volume-imaging speed did not come with a reduction of lateral resolution, with synapses (**Fig. 1d**) clearly resolvable even in single frames taken at 30 Hz (**Supplementary Fig. 2**).

One unique strength of Bessel scanning as a volumetric imaging tool is its robustness against artifacts induced by axial brain motion. In awake, behaving mice, the brain may move both laterally (within the *x–y* plane) and axially (along the *z* axis). Whereas lateral motions can be corrected *post hoc*[6], axial motion correction requires one to constantly image volumes encompassing the entire *z* motion range[7], which may vary from 2 μm (in head-fixed running mice[6]) to 15 μm (induced by licking[7]). Because Bessel foci have an extended axial range for excitation with slow falloff, images taken with Bessel focus scanning are much less sensitive to small *z*-displacements of the sample. In other words, because a Bessel focus is basically light whose lateral spread remains small (as determined by its NA or lateral resolution) over a large axial propagation distance (as indicated by the axial FWHM), during Bessel focus scanning, a volume is imaged with an axial scan speed of the speed of light. As a result, no postprocessing is needed for registration in *z*. As a demonstration, using an extended Bessel focus (NA 0.4, axial FWHM 91 μm), we imaged, at 30 Hz, dendritic branches (180 μm × 180 μm × 160 μm) of a GCaMP6f⁺ neuron in the somatosensory cortex (S1) of an awake mouse. Despite substantial lateral movement, the entire structure stayed within the extended Bessel focus. Simple 2D image registration using the TurboReg[8] plugin for ImageJ was sufficient to register these 30-Hz time-series of 180-μm × 180-μm × 160-μm volumes (**Supplementary Fig. 3a–c** and **Supplementary Video 2**). In another example, we imaged YFP⁺ dendrites in V1 of an awake Thy1-YFP-H mouse that exhibited large brain motion (up to 8-μm lateral displacements; **Supplementary Fig. 3d–h**). After 2D registration, uncorrected axial motions caused substantial fluctuations in the fluorescence signals of two dendrites measured by a Gaussian focus but not in those meas-
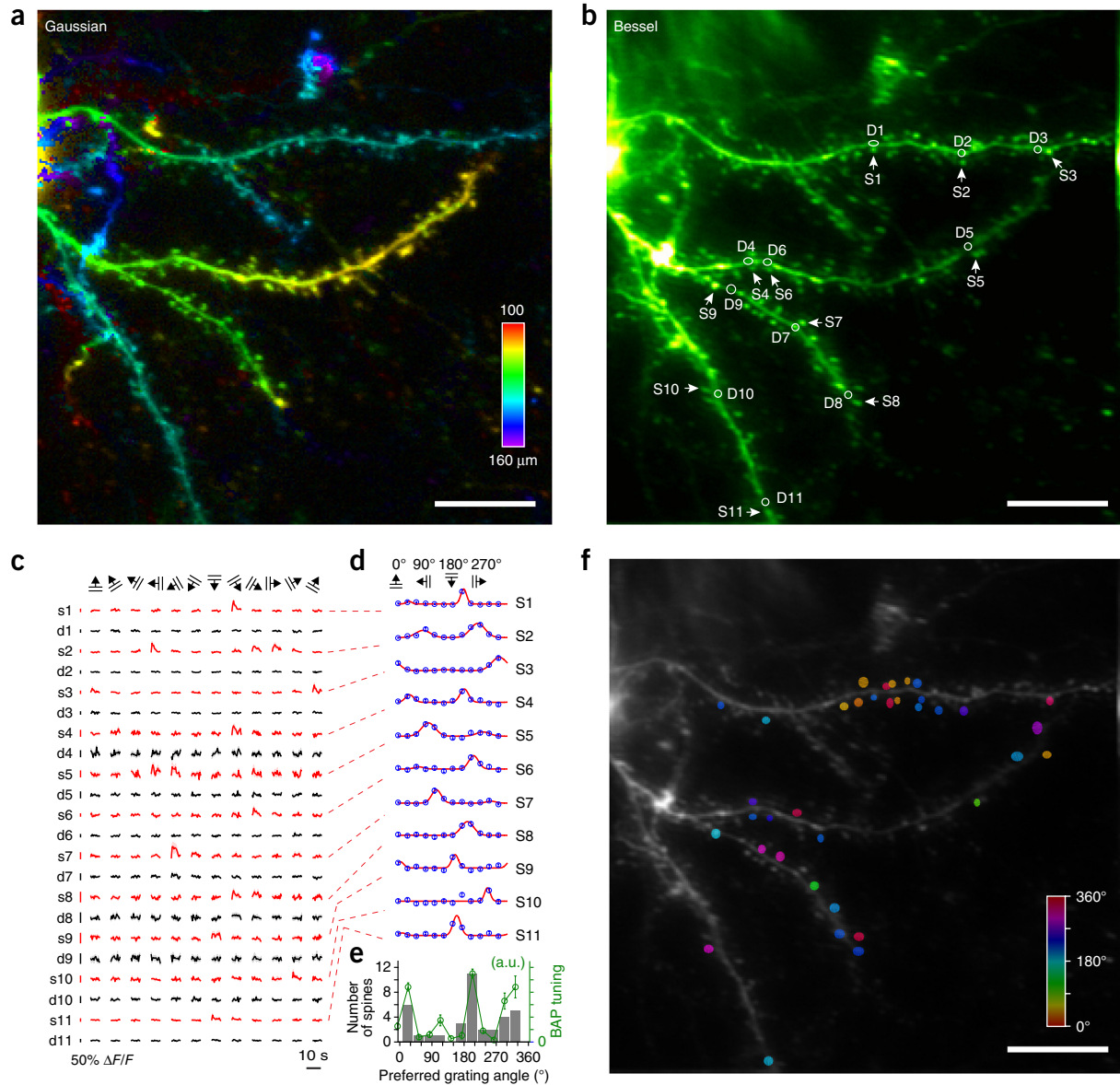
**Figure 2** High-throughput *in vivo* characterization of orientation tuning of dendritic spines in mouse V1. (**a**) Mean intensity projection of a 3D image stack (102 μm × 102 μm × 60 μm) collected by Gaussian focus scanning of dendritic branches (100–160 μm below pia, color-coded by depth) in V1 of an anesthetized mouse. (**b**) Image of the same branches collected by scanning a Bessel focus with 0.4 NA and 35-μm axial FWHM. Example spines (arrowheads, s1–s11) and neighboring dendritic shafts (circles, d1–d11) are indicated. (**c**) Ten-trial-averaged calcium transients of spines (red) and neighboring dendritic shafts (black) in **b** for 12 grating angles. (**d**) Tuning curves of spines from **c**. (**e**) Gray histogram: distribution of preferred grating angles of all tuned spines; green line and circles: tuning curve of BAP-induced calcium transient in dendritic branches. All four main branches had similar tuning curves. Only one is shown. (**f**) Locations of all tuned spines, color-coded by their preferred grating angles. Objective, Olympus 25× with 1.05 NA; postobjective power, 33 mW for Gaussian scanning and 74 mW for Bessel scanning; wavelength, 960 nm; scale bars, 20 μm. Data in **c**, **d** and **e** are averages of ten trials with shadow (**c**) and error bars (**d** and **e**) representing s.e.m.

ured by a Bessel one (NA 0.4, axial FWHM 19 μm; **Supplementary Fig. 3g,h** and **Supplementary Video 3**).

## High-throughput volumetric functional mapping of single spines in mouse and ferret V1

Having demonstrated the feasibility of rapid volumetric imaging of dendritic spines using Bessel foci, we applied this technique to high-throughput functional mapping of sensory-evoked calcium transients in single spines. Because of their small sizes and three-dimensionally distributed locations on dendrites, imaging dendritic spines over large volumes *in vivo* is technically challenging[9]. With conventional

Gaussian focus scanning, multiple imaging planes need to be acquired and tiled to cover a single branch[10,11]. With the extended depth of focus offered by Bessel foci, we could image calcium transients in dendritic spines along multiple dendritic branches simultaneously.

We first investigated the tuning properties of spines on a neuron in V1 layer 2/3 (L2/3) of an anesthetized mouse presented with drifting grating stimuli (12 orientations presented with pseudorandom sequences for 10 trials). Conventional Gaussian focus scanning in 3D provided a depth-resolved image stack of GCaMP6s⁺ spines along dendritic branches 100–160 μm below pia (**Fig. 2a**). Scanning a Bessel focus (NA 0.4, axial FWHM 35 μm) in 2D in a homebuilt microscope,

we resolved these spines in a 102 µm × 102 µm × 60 µm volume (**Fig. 2b**) and measured their visually evoked spine-specific calcium transients at 1.5 Hz (**Supplementary Video 4**). Following previous work[11], we removed transients induced by the occasional back-propagating action potential (BAP) from the calcium signal and quantified the spine calcium transients as percentage fluorescence change $\Delta F/F$ ($\Delta F = F_{response} - F_{baseline}$; $F = F_{baseline}$). Of all 75 identified dendritic spines, 57.3% (43 spines) exhibited visually evoked activity ($\Delta F/F >$ 10%), with 36 spines also showing significant tuning to grating angles ($P < 0.01$, one-way ANOVA across 12 directions; Online Methods). Representative spines showed large visually evoked transients selective to grating angle (**Fig. 2c,d**) but independent of their neighboring dendritic shafts, which showed small responses (**Fig. 2c**). We found that spines on the same branch could have different tuning preferences (**Fig. 2e,f**) and that the tuning curve of the BAP-induced calcium transients in dendritic shafts (indicative of somatic tuning) was similar to the histogram of the preferred grating angles of all tuned spines (**Fig. 2e**), consistent with previous observations[10,11].

As a demonstration that the Bessel scanning module is also compatible with commercial systems, we integrated a Bessel scanning module into a commercial 2PLSM system that images ferret brains[12]. With this system, we achieved similar imaging performance and measured calcium transients from dendrites and spines distributed over a 72-µm axial range within ferret V1 at 30 Hz and determined the tuning of dendritic spines toward drifting gratings (**Supplementary Fig. 4**).

## Population dynamics of inhibitory neuron ensembles in V1 of awake mice

In addition to monitoring the activity of neuronal compartments, Bessel focus scanning can also be used to monitor the population dynamics of 3D neural ensembles, such as cortical GABAergic neurons. These typically inhibitory neurons represent 15–20% of all neurons in neocortex and play important roles in shaping the functional architecture of cortical networks[13]. 2PLSM has been used to study their dynamics *in vivo*[14–16]. Improved labeling strategies (through transgenic mouse strains[17–20] or *post hoc* identification via immunohistochemistry[21]) have enabled imaging of specific subtypes of GABAergic neurons *in vivo*. However, the ensemble dynamics of GABAergic neurons are much less studied. One technical challenge for studying cell-type-specific ensemble activity is caused by their low density in neocortex: a typical 2D image plane may contain <10 GABAergic neurons[14,16,21] and even fewer neurons of specific subtypes[17,19–21], making it difficult to measure the activity of large numbers of neurons at the same time. Using an extended Bessel focus (NA 0.4, axial FWHM 78 µm), we simultaneously captured the calcium transients of up to 71 GCaMP6s+ GABAergic neurons scattered within 256-µm × 256-µm × 100-µm volumes (0–100, 101–200, 201–300 and 301–400 µm below pia) in V1 of quietly awake Gad2-IRES-Cre mice[18]. Due to their low density, almost all neurons visible in the Gaussian 3D stacks could be identified in the projected volume view offered by Bessel focus scanning (**Fig. 3a,b**).

We measured how these GABAergic neurons responded to drifting grating stimuli. During experiments, we also monitored the pupil of the mouse, whose size fluctuations reflected the mouse's brain state[22]. After subtracting the neuropil background[23] from GCaMP6s+ neurites (Online Methods and **Supplementary Fig. 5**), we found that, at all depths, a substantial fraction of neurons were not visually driven but had calcium transients strongly correlated with the pupil size and with each other (**Fig. 3c,d** and **Supplementary Table 3**). Such activity synchrony persisted in darkness (**Supplementary Fig. 6**) and was also observed using the conventional Gaussian focus scanning

mode (**Supplementary Fig. 7**). We found more widespread synchrony for superficial GABAergic neurons than for deeper ones. Calculating Pearson's correlation coefficient $R$ for pairs of neurons, we found that GABAergic neurons 0–200 µm below pia ($n = 348$; a total of 9,672 neuron pairs) had 41% of $R$-values larger than 0.4, whereas neurons 201–400 µm below pia ($n = 383$; a total of 12,809 neuron pairs) only had 22% of all $R$-values larger than 0.4 (**Fig. 3e**).

Because GABAergic neurons in cortex include several subtypes with distinct properties[13], we investigated how activity synchrony depended on cell type. We focused on two subtypes that were immunoreactive for vasoactive intestinal peptide (VIP) and somatostatin (SOM), respectively, because they were known to be involved in cortical state changes as indicated by pupil size[22,24]. Using transgenic mice[18] (VIP-IRES-Cre and SST-IRES-Cre) in which only VIP+ or SOM+ neurons expressed GCaMP6s, we imaged ensembles of VIP+ and SOM+ neurons using Bessel scanning during visual stimulus presentation (**Fig. 3g,l**; see **Fig. 3f,k** for Gaussian 3D stacks). We found that VIP+ neurons ($n = 159$) had highly synchronized activity that was positively correlated with pupil size (60% of 2,185 neuron pairs had $R > 0.4$; **Fig. 3h–j**). In contrast, responses of SOM+ neurons ($n = 136$) were more heterogeneous and, on the population level, less synchronized with pupil size (22% of 1,615 neuron pairs had $R > 0.4$; **Fig. 3m–o**).

These observations are in general agreement with known properties of VIP+ and SOM+ neurons. Earlier *in vivo* studies[20,24] found that individual VIP+ neurons became active during heightened attention and/or pupil dilation, consistent with our observation of large $R$-values between neuronal calcium transients of VIP+ neurons and pupil size (**Fig. 3i,j**). Bessel scanning enabled us to obtain, to our knowledge, the first experimental evidence that VIP+ neuron ensembles in cortical volumes have highly synchronized, brain-state-correlated activity (possibly mediated by gap junctions[25]). Given several recent studies showing that VIP+ neurons directly inhibit SOM+ neurons, we expected to see mostly negative correlation between SOM+ neurons and pupil size. However, we found that SOM+ neurons exhibited heterogeneous responses, with some negatively correlated with pupil size (and thus VIP+ neuron activity) while others positively correlated with pupil size (**Fig. 3m–o**). This is consistent with results from recent *in vivo* studies[24,26], in which SOM+ neurons were found to have heterogeneous population responses, including those coactive with VIP+ neurons. It is also consistent with the suggestion that SOM+ neurons in SST-IRES-Cre mice may include multiple subtypes of inhibitory neurons[27]. The distinct activity patterns of VIP+ and SOM+ neurons may explain the decrease in activity synchrony of GABAergic neurons with depth (**Fig. 3d,e**). Because VIP+ neurons are more abundant in superficial layers whereas SOM+ neurons are more frequently found at larger depths[18,28], the correlation coefficients of the mixed GABAergic populations would be expected to decrease with depth, as observed in our experiment. Finally, the ability of Bessel focus scanning to monitor the activity of inhibitory neuron ensembles in large volumes makes it a powerful tool to elucidate how these neurons shape the dynamics of cortical activity during learning, as well as during distinct attentional and behavior states.

## 30-Hz volumetric imaging of spinal projection neurons in zebrafish larvae

In addition to mammalian brains, Bessel focus scanning can also be applied to other model systems. Even for optically transparent brains such as those of zebrafish larvae, in which widefield imaging methods can image volumes at high rates[29–31], the Bessel approach still offers superior volumetric imaging performance if the neural ensembles
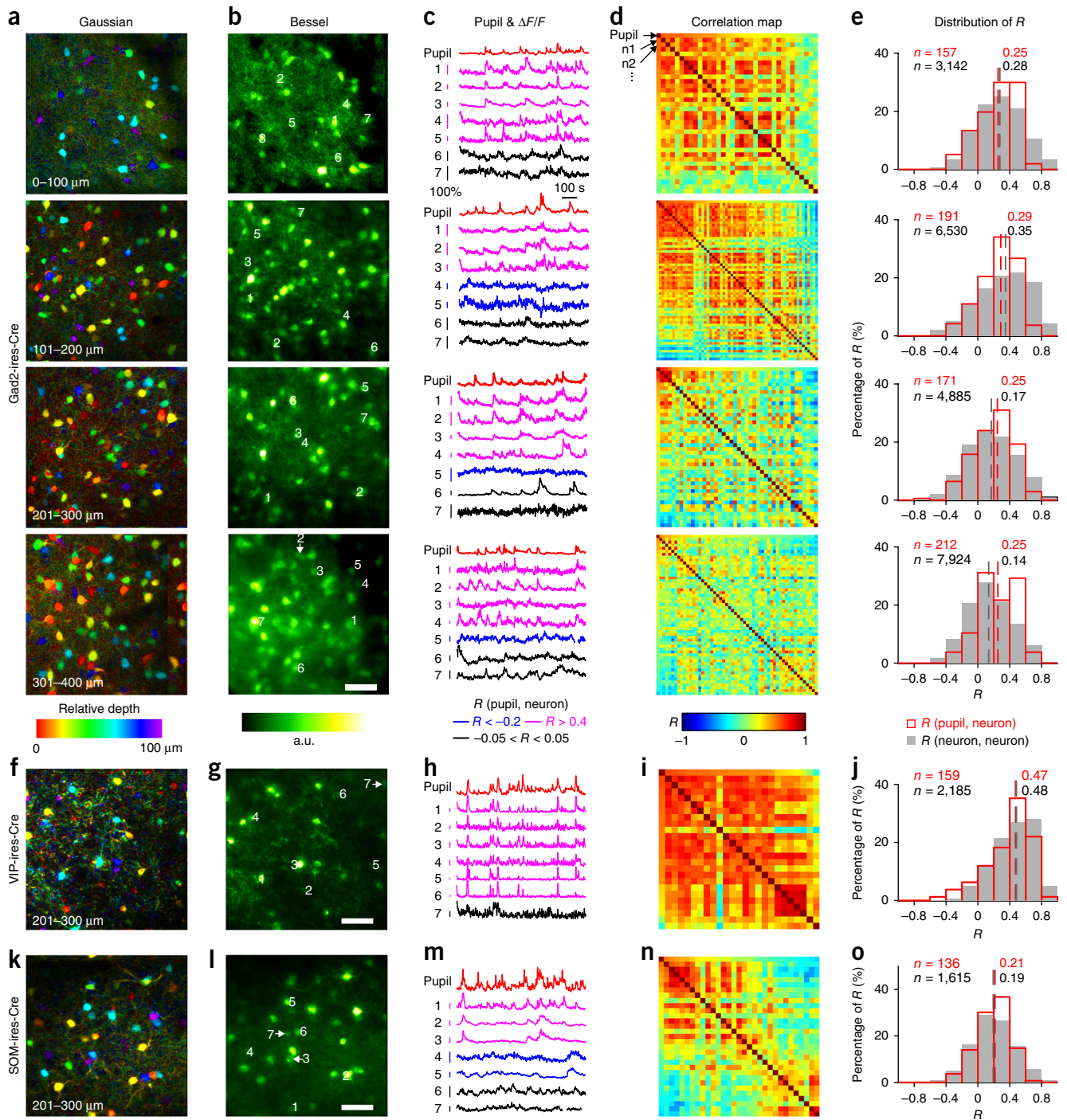
**Figure 3** Activity synchrony among GABAergic neural ensembles in V1 of awake mice. (**a–e**) Measurements on Gad2-IRES-Cre mice transfected with AAV-Syn-Flex-GCaMP6s. (**a**) Mean intensity projections of 3D volumes of neurons (256 μm × 256 μm × 100 μm each; 0–100, 101–200, 201–300, 301–400 μm below pia; 400 two-dimensional images, color-coded by depth) collected by scanning a Gaussian focus in V1. Postobjective power: 5, 5, 11 and 14 mW, respectively. (**b**) Images of the same neurons collected by scanning a Bessel focus at 0.4 NA and 78 μm axial FWHM. Postobjective power: 21, 25.2, 31.5 and 42 mW, respectively. (**c**) Pupil size (red) and concurrently measured calcium transients of neurons numbered in **b** (blue, Pearson's correlation coefficient $R < -0.2$; black, $-0.05 < R < 0.05$; magenta, $R > 0.4$). (**d**) $R$-values between pupil size and calcium transients (first row and first column, neurons sorted in order of descending $R$) and between the calcium transients of all pairs of neurons identifiable in **b**. (**e**) Distribution of $R$ within four depth ranges measured from three mice ($n$, number of $R$-values; red open histogram, $R$ between pupil size and neuronal calcium transients; gray filled histogram, $R$ between neurons; dashed lines, medians). (**f–o**) Measurements and analysis on (**f–j**) VIP-IRES-Cre and (**k–o**) SST-IRES-Cre mice transfected with AAV-Syn-Flex-GCaMP6s. Histograms in **j** and **o** include all VIP+ and SOM+ neurons 1–400 μm below pia. Objective, Olympus 25× with 1.05 NA; wavelength, 960 nm; scale bars, 50 μm.
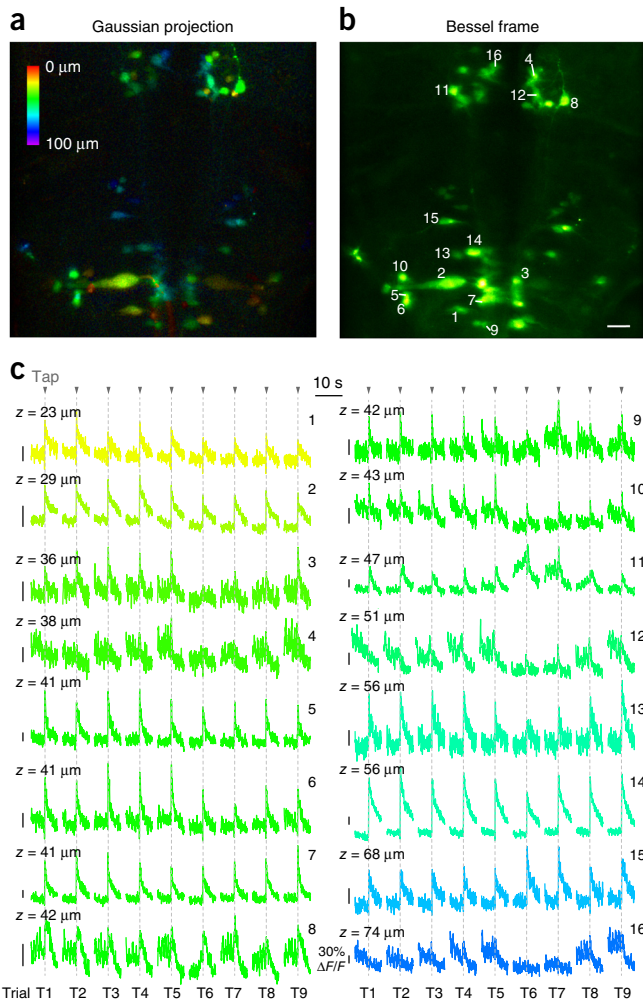
**Figure 4** 30-Hz volumetric imaging of spinal projection neurons in zebrafish larvae. (**a**) Mean intensity projection of a 3D volume (270 μm × 270 μm × 100 μm, 100 two-dimensional images) of retrogradely labeled reticulospinal neurons (color-coded by depth) collected by scanning a Gaussian focus in the hindbrain of a zebrafish larva. Postobjective power, 27 mW. (**b**) Image of the same neurons collected by scanning a Bessel beam with 0.4 NA and 64-μm axial FWHM. Postobjective power, 78 mW. (**c**) Calcium transients of individual neurons numbered in **b** during nine repeated presentations (trial T1 to T9) of a 4-ms mechanical and acoustic stimulus (tap). Traces color-coded by depth of neuron. Objective, Olympus 25× with 1.05 NA; wavelength, 920 nm; scale bar, 20 μm.

the calcium dynamics of the retrogradely labeled reticulospinal neurons in paralyzed larvae (7 d after fertilization) in response to a 4-ms mechanical and acoustic stimulus that induces fictive escape behavior (Online Methods). Unlike using conventional imaging, in which neurons on different $z$ planes would have had to be interrogated separately[35,38], using a Bessel focus (NA 0.4, axial FWHM 64 μm) enabled us to image the reticulospinal neurons within a 270-μm × 270-μm × 100-μm volume at 30 Hz (**Supplementary Video 5**). Due to minimal overlap between these neurons when viewed dorsally, all the neurons visible in the conventionally obtained $z$ stack (**Fig. 4a**) were identifiable in the projected volume view offered by the Bessel focus scan (**Fig. 4b**). During nine repeated presentations of the stimulus (**Fig. 4c**), most neurons showed stimulus-evoked calcium transients, consistent with previous recordings during escape behavior[35]. Additionally, bursts of activity were observed between stimulus presentations in sets of neurons that were distinct from, but overlapping with, those activated by the stimulus (**Fig. 4c**). The ability to monitor the activity of neurons located at different depths simultaneously made it possible to detect trial-to-trial variations in the ensemble activity and to discover neurons with correlated or anticorrelated activity patterns (**Fig. 4c**).

## Characterization of visually evoked responses in sparsely as well as densely labeled fruit fly brains

The fruit fly (*Drosophila melanogaster*) is an important model organism for the field of neuroscience. The availability of sophisticated genetic tools and the small size of the fly brain have made it possible to record activity from anywhere inside the brain[39,40]. We first used Bessel focus scanning to image GCaMP6f[+11] neurites in UAS-GCaMP6f;33A12-GAL4 flies[41] (Online Methods). Presenting the same drifting grating stimuli described above to head-fixed flies (**Fig. 5a,b**), we monitored the calcium dynamics of a volume of neurites comprising most of the central complex (190 μm × 95 μm × 60 μm; **Fig. 5b**), a highly structured neuropil in the center of the fly brain, at a rate of 2.5 Hz, using Bessel focus (NA 0.4, axial FWHM 35 μm) scanning. The imaged volume contained fine neurites surrounding the ellipsoid body (a substructure of the central complex; **Fig. 5c**), whose activity can be captured by a single Bessel frame (**Fig. 5d**). We found that the columnar neuron neurites within the ellipsoid body on either side of the central complex midline (**Fig. 5d**) had strongly anticorrelated activity ($R = -0.73$; **Fig. 5e**) that was not synchronized to the presentation of visual stimulation. In contrast, two neuronal processes above the ellipsoid body on both sides of the midline were strongly activated by drifting grating stimuli with no preference with respect to grating orientation (**Fig. 5f** and **Supplementary Video 6**).

We also applied Bessel focus scanning to fly brains with panneuronal expression of GCaMP6f (UAS-GCaMP6f;57C10-GAL4)[41]. Scanning with an extended Bessel focus (NA 0.4, axial FWHM 78 μm) allowed us to measure visually evoked responses from a 307-μm × 216-μm × 100-μm volume (**Fig. 5g,h**), ~25% of the entire adult brain, at 3.6 Hz. Notably, the pixels with the strongest responses to grating stimuli in our imaging volume (**Fig. 5h,i** and **Supplementary Video 7**) fell within the area of the mushroom bodies, structures mostly known for olfactory learning and memory but not for visually driven responses in *Drosophila*. Because Bessel focus scanning cannot resolve structures along the $z$ direction, we switched the microscope to conventional scanning with a Gaussian focus to confirm these responses. Placing the Gaussian focus within the mushroom bodies (**Fig. 5j**) and presenting the fly with the same grating stimuli, we again observed visually driven responses in the mushroom bodies (**Fig. 5k** and **Supplementary Video 8**). Both the axially averaged responses

under investigation are distributed sparsely in 3D. One example is the set of spinal projection neurons in the hindbrain of zebrafish larvae. These neurons, which form a stereotyped array in which many cells are uniquely identifiable across individuals[32], are responsible for the descending control of swimming behaviors, including sensory-evoked escapes[33]. While some of these neurons appear to be dedicated to controlling specific movements[33], there is evidence for modules that control different kinematic features across behaviors[34], as well as for more distributed control of swim kinematics[35]. We do not yet have an integrated understanding of how this population controls swimming. Since larval swimming occurs in discrete bouts separated by as little as 100 ms, relating activity in this population to behavior will require imaging simultaneously across all the neuronal groups with high temporal resolution. We injected Cal520 dextran into the ventral spinal cord[36] of *mitfa*^{−/−} (nacre)[37] zebrafish. We then examined
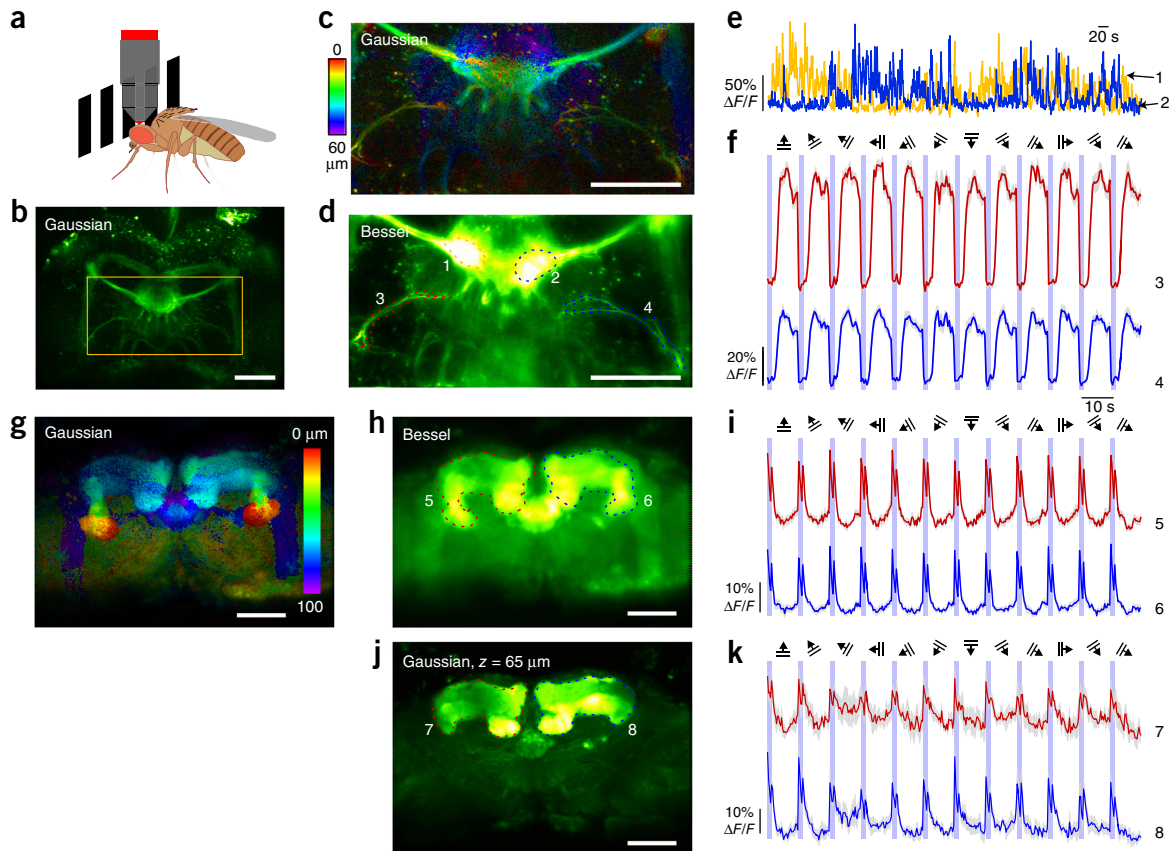
**Figure 5** *In vivo* volumetric functional imaging of fruit fly brains responding to visual stimuli. (**a**) Brains of head-fixed flies were imaged during the presentation of grating stimuli. (**b**) *In vivo* image of the brain of a UAS-GCaMP6f;33A12-GAL4 fly (mean intensity projection of a 60-µm volume). (**c**) Mean intensity projection of a 3D volume (190 µm × 95 µm × 60 µm, 61 two-dimensional images) within the orange rectangle in **b** of GCaMP6f⁺ neurites (color-coded by depth) with Gaussian focus scanning. Postobjective power, 14 mW. (**d**) Image of the same neurites collected by scanning a Bessel beam with 0.4 NA and 35 µm axial FWHM. Postobjective power, 82 mW. (**e**) Neurites within the left and right lobes of the ellipsoid body (numbered 1 and 2 in **d**) showed anticorrelated calcium activity. (**f**) Ten-trial-averaged calcium transients of two neurites (numbered 3 and 4 in **d**) strongly driven by grating visual stimuli. (**g**) Mean intensity projection of a 3D volume (307 µm × 216 µm × 100 µm; 101 two-dimensional images, color-coded by depth) of a GCaMP6f;57c10-GAL4 fly with pan-neuronal expression of GCaMP6f with Gaussian focus scanning. Postobjective power, 11 mW. (**h**) Image of the same brain collected by scanning a Bessel beam with 0.4 NA and 78 µm axial FWHM. Postobjective power, 31.5 mW. (**i**) Calcium transients (ten-trial-averaged) from areas numbered 5 and 6 in **h** were evoked by both the appearance of a static grating (data points within purple stripes) and the onset of its drifting movement (data points after purple stripes). (**j**) Optically sectioned image at *z* = 65 µm collected by Gaussian focus scanning. Bright structures are the left and right lobes of the mushroom body. (**k**) Optically sectioned responses (ten-trial-averaged) in mushroom body (areas numbered 7 and 8 in **j**) shared similar temporal dynamics to the axially averaged responses in **i**. Objective, Olympus 25× with 1.05 NA; wavelength, 940 nm; scale bars, 50 µm. Shadows in **h**–**k** represent s.e.m. across trials.

obtained via Bessel focus scanning and the optically sectioned responses obtained via conventional scanning shared similar features: calcium transients were evoked by both the appearance of new stationary gratings and the drifting movement of the gratings, and in both cases, the transients rapidly decayed with time. Our observation that mushroom bodies exhibit visually evoked responses is consistent with the recent discovery of Kenyon cells in the mushroom body that selectively respond to visual stimulation[42]. Given that the adult fly brain has a lateral extension (590 µm × 340 µm) that fits within the typical field of view of 2PLSM and a thickness (120 µm) that fits within the axial extent of our Bessel foci, Bessel focus scanning shows great promise as a method for rapid surveys of stimulus- or behavior-related neural activity in the entire fly brain.

## DISCUSSION

To understand information processing in neurons and neural networks that extend in three dimensions, we need to record neural activity at a subsecond volume rate, while ideally maintaining the

lateral resolution to resolve synapses. Taking advantage of the fact that, during most *in vivo* brain imaging experiments, the structures of interest are stationary, we obtained volume information by scanning in 2D an axially extended focus approximating a Bessel beam. Using Bessel foci optimized to maintain high lateral resolution *in vivo*, we imaged the brains of a variety of species, including fruit fly, zebrafish, mouse and ferret, and demonstrated high-speed volumetric imaging of neurons and neural compartments *in vivo*. The idea of extended depth-of-field imaging dates back 50 years[2], and axially extended Bessel foci have been combined with 2PLSM to image brain slices[4,5]. In our work, we systematically characterized the *in vivo* imaging performance of Bessel foci of different NAs and lengths, and we found that low-NA Bessel foci provided optimal performance. Preserving submicron, synapse-resolving lateral resolution while reducing the background generated by the outer rings, these Bessel foci enabled us to measure calcium activity from single spines on multiple dendritic branches at 30 Hz, a combination of resolution and speed that is not matched by other volume imaging methods. Even though this performance

came with the sacrifice of axial resolution, given sufficient signal-to-noise ratio, axial resolution could be recovered during Bessel focus scanning through parallax-based stereo microscopy[3,5,43].

Now that we have discovered the optimal Bessel foci for *in vivo* extended depth-of-field imaging, a technical discussion on the best way to generate them is in order. The most common method for generating a Bessel focus is by using an axicon (conical lens). Compared to our module, which employs an SLM, axicon-based systems are less expensive[4,5], but they can only generate a Bessel focus with fixed NA and axial length. For experiments requiring various combinations of NA and length, an SLM-based module is preferable, due to its flexibility and versatility. Furthermore, in addition to its ability to generate longer Bessel foci than axicons[3], an SLM may also shape the axial intensity profile. For example, using an SLM, we generated a Bessel focus with a higher intensity at larger depth, which improved image quality for deeper structures by compensating for the scattering loss of the excitation light (**Supplementary Fig. 8**).

Regardless of how a Bessel focus is generated, once incorporated into a microscope, the volume imaging speed depends on the lateral scanning speed of the microscope, with a 30-Hz volume rate at $512 \times 512$ lateral pixels easily achievable in systems equipped with resonant galvanometers, as demonstrated here. With these systems, much higher volume speed can be achieved by simply reducing the number of lateral pixels. Ultimately, with heating and photodamage of the brain placing an upper limit on excitation power, the practically achievable volume imaging speed depends on the fluorescence probe, with brighter probes requiring less dwell time at each pixel and thus enabling higher imaging speed.

What is the limit on the axial extent of the volume? The longest Bessel focus that we generated to image brains *in vivo* was 400 µm at 0.4 NA (data not shown). Even though longer Bessel foci can be generated by the SLM, the practically useful axial length is determined by both the sample and the desired lateral resolution. Sparsely labeled samples have lower probability of having structures overlap in their *x*–*y* locations and thus allow longer foci to be used. However, at the same NA, longer Bessel foci have more energy in the side rings surrounding the central peak[44], which may lead to higher background signal (**Supplementary Fig. 1**). Relaxing the lateral resolution requirement further (for example, from submicron, synaptic resolution to cellular, micron-level resolution) would allow lower-NA Bessel foci to be employed, where background contamination by the side rings is less of an issue. Another practical limitation on the length of the Bessel focus is optical power. In general, compared to Gaussian focus scanning, the redistribution of power into the side rings during the formation of a Bessel focus requires the average excitation power to be increased. For large structures such as somata, because the axial extension of the Bessel focus allows a larger volume of fluorophores to be excited, the power increase may be minimal: for example, for functional imaging experiments of GABAergic neurons at 0–100 µm depth, we used 21 mW postobjective power for Bessel focus (**Fig. 3a**) and 14–18 mW for Gaussian focus (**Supplementary Fig. 7**). Smaller structures such as dendritic spines require higher power increases (for example, 1.5–4×), and care needs to be taken to ensure that the physiology of the brain is not altered by the introduced laser power. However, because in a Bessel focus the extra power is distributed broadly in the side rings rather than in the central peak, photo-induced damages involving higher-order nonlinear processes should not be much more severe than in a Gaussian focus. Given that photodamage causes the basal fluorescence of calcium indicators to increase[45], the fact that none of the GCaMP6$^+$ neurons imaged with Bessel focus mode showed basal fluorescence increase suggests that photodamage was indeed

not a concern with the power used here. In terms of heating-induced effects, the average power used in our experiment was still within the safe range[46].

The application of Bessel focus scanning is not limited to neurons. Any sample with sparsely labeled stationary structures can be imaged at high volume rates using this approach. A useful rule of thumb is that if the volumetric structures of interest can be visualized by the mean intensity projection of their Gaussian image stack, Bessel focus scanning can be applied. For densely labeled brains, Bessel scanning can be used as a high-throughput screening method to identify areas of activity followed by investigations at higher axial resolution (**Fig. 5g–k**). For studies of densely labeled brains in which single-neuron resolution is required, Bessel scanning may also be applied if the activity pattern is sparse and if spatially overlapping calcium responses can be unmixed temporally[47,48]. It is important to note, however, due to the much more extended axial excitation by Bessel focus, calcium signals measured in Bessel focus scanning mode may contain more substantial contributions from neuropils expressing calcium indicators[23]. These neuropil contaminations need to be carefully removed (**Supplementary Fig. 5**) and any observed correlation in neural activity confirmed with Gaussian focus scanning whenever possible. Nuclear-targeted calcium indicators may be used to further eliminate this complication, in which case an upper limit of neural density may be estimated (**Supplementary Technical Note**).

In addition to the fact that video-rate volume imaging with synaptic lateral resolution, as reported here, has not been demonstrated by other methods, Bessel focus scanning has several advantages when compared to other volumetric imaging methods. Compared to microscopy methods based on light-sheet excitation and widefield detection[29–31], our method employs two-photon excitation and nonimaging detection, which allows it to be applied to more opaque mammalian brains. Compared to volume imaging methods that rapidly move a Gaussian focus in 3D[49] (**Supplementary Table 4**), by projecting 3D volume information into 2D, Bessel focus scanning leads to a ten- to hundred-fold reduction in data size and orders-of-magnitude increases in image throughput (**Supplementary Table 2**). In addition, unlike other methods, Bessel focus scanning can be integrated into existing microscope systems without any change to the data acquisition hardware or software. (In our experiments, Bessel modules were added to two homebuilt and one commercial systems run by three different control software packages: homemade, open source[50] and commercial, respectively). Its intrinsic insensitivity to sample *z* motion also makes this extended depth-of-field approach uniquely suitable for *in vivo* volume imaging in awake preparations. Finally, the Bessel module can be combined with existing scanning hardware (for example, galvanometers, acousto-optical deflectors, fast axial scanning units) and modes (for example, raster scanning, line scanning, random accessing) to achieve higher speed, larger volume and more versatile experiments to study brains in action.

## METHODS

Methods, including statements of data availability and any associated accession codes and references, are available in the online version of the paper.

*Note: Any Supplementary Information and Source Data files are available in the online version of the paper.*

**AUTHOR CONTRIBUTIONS**

N.J. conceived and oversaw the project; R.L. and N.J. designed the Bessel modules; R.L. and N.J. built Bessel modules with help from A.K., W.S., B.M., D.E.W. and B.S.; W.S. and Y.L. prepared mouse samples; R.L., W.S., Y.L., A.K., B.M. and N.J. collected mouse data; M.K. and M.B.O. designed zebrafish experiments; J.B. prepared zebrafish samples with help from M.T.; R.L., A.K., J.B. and N.J. collected zebrafish data; J.D.S., R.L. and N.J. designed *Drosophila* experiments; J.D.S. prepared *Drosophila* samples; R.L., J.D.S. and N.J. collected *Drosophila* data; D.F. and N.J. designed ferret experiments; and D.E.W. and B.S. prepared ferret samples and collected ferret data. All authors contributed to data analysis and presentation. R.L. and N.J. wrote the paper with inputs from all authors.

**COMPETING FINANCIAL INTERESTS**

The authors declare no competing financial interests.

Reprints and permissions information is available online at http://www.nature.com/reprints/index.html.

1. Denk, W., Strickler, J.H. & Webb, W.W. Two-photon laser scanning fluorescence microscopy. *Science* **248**, 73–76 (1990).
2. Welford, W.T. Use of annular apertures to increase focal depth. *J. Opt. Soc. Am.* **50**, 749–753 (1960).
3. Botcherby, E.J., Juškaitis, R. & Wilson, T. Scanning two photon fluorescence microscopy with extended depth of field. *Opt. Commun.* **268**, 253–260 (2006).
4. Thériault, G., De Koninck, Y. & McCarthy, N. Extended depth of field microscopy for rapid volumetric two-photon imaging. *Opt. Express* **21**, 10095–10104 (2013).
5. Thériault, G., Cottet, M., Castonguay, A., McCarthy, N. & De Koninck, Y. Extended two-photon microscopy in live samples with Bessel beams: steadier focus, faster volume scans, and simpler stereoscopic imaging. *Front. Cell. Neurosci.* **8**, 139 (2014).
6. Dombeck, D.A., Khabbaz, A.N., Collman, F., Adelman, T.L. & Tank, D.W. Imaging large-scale neural activity with cellular resolution in awake, mobile mice. *Neuron* **56**, 43–57 (2007).
7. Andermann, M.L., Kerlin, A.M. & Reid, R.C. Chronic cellular imaging of mouse visual cortex during operant behavior and passive viewing. *Front. Cell. Neurosci.* **4**, 3 (2010).
8. Thévenaz, P., Ruttimann, U.E. & Unser, M. A pyramid approach to subpixel registration based on intensity. *IEEE Trans. Image Process.* **7**, 27–41 (1998).
9. Jia, H., Rochefort, N.L., Chen, X. & Konnerth, A. Dendritic organization of sensory input to cortical neurons in vivo. *Nature* **464**, 1307–1312 (2010).
10. Chen, X., Leischner, U., Rochefort, N.L., Nelken, I. & Konnerth, A. Functional mapping of single spines in cortical neurons in vivo. *Nature* **475**, 501–505 (2011).
11. Chen, T.-W. *et al.* Ultrasensitive fluorescent proteins for imaging neuronal activity. *Nature* **499**, 295–300 (2013).
12. Wilson, D.E., Whitney, D.E., Scholl, B. & Fitzpatrick, D. Orientation selectivity and the functional clustering of synaptic inputs in primary visual cortex. *Nat. Neurosci.* **19**, 1003–1009 (2016).
13. Kubota, Y. Untangling GABAergic wiring in the cortical microcircuit. *Curr. Opin. Neurobiol.* **26**, 7–14 (2014).
14. Sohya, K., Kameyama, K., Yanagawa, Y., Obata, K. & Tsumoto, T. GABAergic neurons are less selective to stimulus orientation than excitatory neurons in layer II/III of visual cortex, as revealed by in vivo functional Ca2+ imaging in transgenic mice. *J. Neurosci.* **27**, 2145–2149 (2007).
15. Liu, B.H. *et al.* Visual receptive field structure of cortical inhibitory neurons revealed by two-photon imaging guided recording. *J. Neurosci.* **29**, 10520–10532 (2009).
16. Kameyama, K. *et al.* Difference in binocularity and ocular dominance plasticity between GABAergic and excitatory cortical neurons. *J. Neurosci.* **30**, 1551–1559 (2010).
17. Runyan, C.A. *et al.* Response features of parvalbumin-expressing interneurons suggest precise roles for subtypes of inhibition in visual cortex. *Neuron* **67**, 847–857 (2010).
18. Taniguchi, H. *et al.* A resource of Cre driver lines for genetic targeting of GABAergic neurons in cerebral cortex. *Neuron* **71**, 995–1013 (2011).
19. Polack, P.-O., Friedman, J. & Golshani, P. Cellular mechanisms of brain state-dependent gain modulation in visual cortex. *Nat. Neurosci.* **16**, 1331–1339 (2013).
20. Fu, Y. *et al.* A cortical circuit for gain control by behavioral state. *Cell* **156**, 1139–1152 (2014).
21. Kerlin, A.M., Andermann, M.L., Berezovskii, V.K. & Reid, R.C. Broadly tuned response properties of diverse inhibitory neuron subtypes in mouse visual cortex. *Neuron* **67**, 858–871 (2010).
22. McGinley, M.J. *et al.* Waking state: rapid variations modulate neural and behavioral responses. *Neuron* **87**, 1143–1161 (2015).
23. Göbel, W. & Helmchen, F. In vivo calcium imaging of neural network function. *Physiology (Bethesda)* **22**, 358–365 (2007).
24. Reimer, J. *et al.* Pupil fluctuations track fast switching of cortical states during quiet wakefulness. *Neuron* **84**, 355–362 (2014).
25. Hestrin, S. & Galarreta, M. Electrical synapses define networks of neocortical GABAergic neurons. *Trends Neurosci.* **28**, 304–309 (2005).
26. Pakan, J.M.P. *et al.* Behavioral-state modulation of inhibition is context-dependent and cell type specific in mouse visual cortex. *eLife* **5**, e14985 (2016).
27. Hu, H., Cavendish, J.Z. & Agmon, A. Not all that glitters is gold: off-target recombination in the somatostatin-IRES-Cre mouse line labels a subset of fast-spiking interneurons. *Front. Neural Circuits* **7**, 195 (2013).
28. Pfeffer, C.K., Xue, M., He, M., Huang, Z.J. & Scanziani, M. Inhibition of inhibition in visual cortex: the logic of connections between molecularly distinct interneurons. *Nat. Neurosci.* **16**, 1068–1076 (2013).
29. Ahrens, M.B., Orger, M.B., Robson, D.N., Li, J.M. & Keller, P.J. Whole-brain functional imaging at cellular resolution using light-sheet microscopy. *Nat. Methods* **10**, 413–420 (2013).
30. Panier, T. *et al.* Fast functional imaging of multiple brain regions in intact zebrafish larvae using selective plane illumination microscopy. *Front. Neural Circuits* **7**, 65 (2013).
31. Bouchard, M.B. *et al.* Swept confocally-aligned planar excitation (SCAPE) microscopy for high speed volumetric imaging of behaving organisms. *Nat. Photonics* **9**, 113–119 (2015).
32. Kimmel, C.B., Powell, S.L. & Metcalfe, W.K. Brain neurons which project to the spinal cord in young larvae of the zebrafish. *J. Comp. Neurol.* **205**, 112–127 (1982).
33. O'Malley, D.M., Kao, Y.-H. & Fetcho, J.R. Imaging the functional organization of zebrafish hindbrain segments during escape behaviors. *Neuron* **17**, 1145–1155 (1996).
34. Severi, K.E. *et al.* Neural control and modulation of swimming speed in the larval zebrafish. *Neuron* **83**, 692–707 (2014).
35. Gahtan, E., Sankrithi, N., Campos, J.B. & O'Malley, D.M. Evidence for a widespread brain stem escape network in larval zebrafish. *J. Neurophysiol.* **87**, 608–614 (2002).
36. Gahtan, E. & O'Malley, D.M. Rapid lesioning of large numbers of identified vertebrate neurons: applications in zebrafish. *J. Neurosci. Methods* **108**, 97–110 (2001).
37. Lister, J.A., Robertson, C.P., Lepage, T., Johnson, S.L. & Raible, D.W. nacre encodes a zebrafish microphthalmia-related protein that regulates neural-crest-derived pigment cell fate. *Development* **126**, 3757–3767 (1999).
38. Orger, M.B., Kampff, A.R., Severi, K.E., Bollmann, J.H. & Engert, F. Control of visually guided behavior by distinct populations of spinal projection neurons. *Nat. Neurosci.* **11**, 327–333 (2008).
39. Seelig, J.D. *et al.* Two-photon calcium imaging from head-fixed *Drosophila* during optomotor walking behavior. *Nat. Methods* **7**, 535–540 (2010).
40. Weir, P.T. & Dickinson, M.H. Functional divisions for visual processing in the central brain of flying *Drosophila*. *Proc. Natl. Acad. Sci. USA* **112**, E5523–E5532 (2015).
41. Jenett, A. *et al.* A GAL4-driver line resource for *Drosophila* neurobiology. *Cell Rep.* **2**, 991–1001 (2012).
42. Vogt, K. *et al.* Direct neural pathways convey distinct visual information to *Drosophila* mushroom bodies. *eLife* **5**, e14009 (2016).
43. Song, A. *et al.* Volumetric two-photon imaging of neurons using stereoscopy (vTwINS). Preprint at http://www.biorxiv.org/content/early/2016/09/06/073742.
44. Stamnes, J.J., Heier, H. & Ljunggren, S. Encircled energy for systems with centrally obscured circular pupils. *Appl. Opt.* **21**, 1628–1633 (1982).
45. Ji, N., Magee, J.C. & Betzig, E. High-speed, low-photodamage nonlinear imaging using passive pulse splitters. *Nat. Methods* **5**, 197–202 (2008).
46. Podgorski, K. & Ranganathan, G. Brain heating induced by near-infrared lasers during multiphoton microscopy. *J. Neurophysiol.* **116**, 1012–1023 (2016).
47. Yang, W. *et al.* Simultaneous multi-plane imaging of neural circuits. *Neuron* **89**, 269–284 (2016).
48. Pnevmatikakis, E.A. *et al.* Simultaneous denoising, deconvolution, and demixing of calcium imaging data. *Neuron* **89**, 285–299 (2016).
49. Ji, N., Freeman, J. & Smith, S.L. Technologies for imaging neural activity in large volumes. *Nat. Neurosci.* **19**, 1154–1164 (2016).
50. Pologruto, T.A., Sabatini, B.L. & Svoboda, K. ScanImage: flexible software for operating laser scanning microscopes. *Biomed. Eng. Online* **2**, 13 (2003).

# ONLINE METHODS

**Animal use.** All animal experiments were conducted according to the National Institutes of Health guidelines for animal research. Procedures and protocols on mice and zebrafish were approved by the Institutional Animal Care and Use Committee at Janelia Research Campus, Howard Hughes Medical Institute. Experimental protocols on ferrets were approved by the Max Planck Florida Institute for Neuroscience Institutional Animal Care and Use Committee.

**Assembly, incorporation and control of Bessel modules in three 2PLSMs.** A focus approximating a Bessel beam can be generated by illuminating the back pupil plane of a microscope objective with an annular pattern (i.e., a ring). We chose to use a reflective phase-only spatial light modulator (SLM, CODPDM512-800-1000-P8, Meadowlark Optics, 15-μm pixel size) to generate annular illumination, because it allowed us to produce Bessel foci of different NAs and axial lengths and systematically test their imaging performance *in vivo* (**Supplementary Fig. 1**). With the SLM placed at the front focal plane of lens L1, an electric field distribution that was the Fourier transform of the phase pattern on the SLM was generated at the back focal plane of L1[51], where we placed an annular apodization mask to block spurious orders and undiffracted light. The apodization mask was then imaged onto the galvanometers and the back pupil plane of the microscope objective using pairs of lenses (L2 and L3, L4 and L5) in 4*f* configuration (**Fig. 1b**). For ease of alignment, the SLM was mounted on a platform with 3D translational and two-axis rotational controls, and the annular mask was mounted on a 3D translational stage. When incorporating Bessel modules into two home-built 2PLSM in Janelia and one commercial 2PLSM (Thorlabs) in Max Planck Florida, different lenses were used to match the magnification factor and objective used in each system (**Supplementary Table 1**).

A standalone control program (Meadowlark Optics) displayed phase patterns on the SLM, with no communication with or modification of the microscope software needed. Concentric binary grating patterns on the SLM were used to generate annular illumination at the apodization mask[3] (see **Supplementary Technical Note** and **Supplementary Software** for details). By selecting a specific annulus on an apodization mask array (Photo Sciences, Inc.) to truncate the electric field distribution at the back focal plane of L1, we were able to fine-tune the axial lengths and intensity distributions of the Bessel-like foci (**Supplementary Fig. 9**). (Strictly speaking, a Bessel beam is generated by an infinitely thin annulus, has infinite axial length and carries infinite energy. The Bessel-like foci generated here with annuli of finite widths are known as quasi-Bessel or finite Bessel beams.) The NA of a Bessel focus is dictated by the outer diameter of the annulus, while its axial length depends on the thickness of the annulus, with thinner annuli generating longer Bessel foci. The combination of SLM with the apodization mask array enabled independent adjustments of the NA and axial length of the Bessel focus. Overlaying a defocus pattern on the binary concentric grating, we engineered Bessel foci with higher axial intensities at larger *z* depths to facilitate the imaging of deeper structures in scattering brains (**Supplementary Fig. 8**).

**Mouse preparation.** Mice (females or males, >2 months old) were housed in cages, in groups of 1–5 before surgeries and in pairs or singly housed afterward, under a reversed light cycle. Wild-type mice were used for all mouse experiments except those in **Figure 3**, in which we used Gad2-IRES-Cre (Jackson Laboratories, *Gad2*tm2(cre)Zjh/J, stock #010802), SST-IRES-Cre (Jackson Laboratories, *Sst*<tm2.1(cre)Zjh>/J, stock #013044) and VIP-IRES-Cre (Jackson Laboratories, *Vip*<tm1(cre)Zjh>/J, stock #010908) mice[18] with Cre-dependent GCaMP6s virus injection (AAV2/1.syn.Flex.GCaMP6s, ~8 × 10^{11} infectious units per mL) in V1. Sparse expression of GCaMP6s was achieved by injecting a mixture of diluted AAV2/1-syn-Cre particles (original titer: ~10[12] infectious units per mL, diluted 8,000-fold in phosphate-buffered saline) and high-titer, Cre-dependent GCaMP6s virus (AAV2/1.syn.Flex.GCaMP6s, ~8 × 10^{11} infectious units per ml).

Virus injection and cranial window implantation procedures have been described previously[52]. Briefly, a 2.5-mm diameter craniotomy was made over either V1 or S1 of mice that were anaesthetized with isoflurane (1–2% by volume in O₂) and given the analgesic buprenorphine (SC, 0.3 mg per kg of body weight). Dura was left intact. Virus injection was then performed using a glass pipette (Drummond Scientific Company) beveled at 45° with a 15- to 20-μm opening and backfilled with mineral oil. A fitted plunger controlled by a hydraulic manipulator (Narishige, MO10) was inserted into the pipette and used to load

and slowly inject 10–20 nL viral solution into the brain (~200–400 μm below pia). After the pipette was pulled out of the brain, a glass window made of a single coverslip (Fisher Scientific, no. 1.5) was embedded in the craniotomy and sealed in place with dental acrylic. A titanium headpost was then attached to the skull with cyanoacrylate glue and dental acrylic. *In vivo* imaging was carried out after two weeks of recovery in single or paired housing and habituation for head fixation. All imaging experiments were carried out on headfixed, awake mice, except data in **Figure 2**, for which mice were anesthetized to reduce calcium transients induced by BAP.

**Ferret preparation.** Juvenile female ferrets (*Mustela putorius furo*, Marshall Farms) housed in a vivarium under 16-h light/8-h dark cycle were used. Sterile surgical procedures have been described previously[12]. Briefly, virus injection was carried out in P21–P23 juvenile female ferrets anesthetized with ketamine (50 mg/kg, IM) and isoflurane (1–3% in O₂), then intubated and artificially respired. Atropine (0.2 mg/kg, SC) was administered to reduce secretions. 1:1 mixture of lidocaine and bupivacaine was administered subcutaneously in the scalp. With the internal temperature maintained at 37 °C with a heating pad, a 0.8-mm-diameter craniotomy was made over ferret V1. AAV2/1.hSyn.Cre (1.32 × 10^{13} infectious units per ml, Penn Vector Core) was diluted by 100,000 fold in PBS (Sigma) and mixed with AAV2/1.CAG.Flex.GCaMP6s (7.31 × 10^{12} infectious units per mL, Penn Vector Core) to sparsely express GCaMP6s in layer 2/3 cortical neurons. Beveled glass micropipettes (~15-μm outer diameter) were lowered into the brain, and 55 nL of virus were injected (Nanoject II, Drummond Scientific Company) at 250 and 400 μm below the pia. To prevent dural regrowth and attachment to the arachnoid membrane, the craniotomy was filled with 1% w/v agarose (Type IIIa, Sigma-Aldrich).

After two to three weeks of expression, ferrets were anesthetized with ketamine and isoflurane, administered atropine and bupivacaine, placed on a heating pad, intubated after tracheotomy and artificially respired. An intravenous cannula was placed to deliver fluids. ECG, end-tidal CO₂, external temperature and internal temperature were continuously monitored during the procedure and subsequent imaging session. After scalp retraction, a titanium head plate was adhered to the skull using C&B Metabond (Parkell). A 5.5- to 6.0-mm-diameter craniotomy was performed at the viral injection site and the dura retracted to reveal the cortex. A titanium cannula with a 5.0-mm outer diameter and a glass bottom (affixed with optical adhesive #71, Norland Products) was placed onto the brain to gently compress the underlying cortex and dampen brain motion. The cranial cannula was hermetically sealed using a stainless steel retaining ring (5/16 in or 0.79 cm internal retaining ring, McMaster-Carr), Kwik-Cast (World Precision Instruments) and Vetbond (3M). A 1:1 mixture of 1% Tropicamide ophthalmic solution (Akorn) and 10% phenylephrine hydrochloride ophthalmic solution (Akorn) was applied to both eyes to dilate the pupils and retract the nictitating membranes. Eyes were lubricated hourly with silicon oil AP 150 Wacker (Sigma-Aldrich). Upon completion of the surgical procedure, isoflurane was gradually reduced and then vecuronium (2 mg/kg/h) or pancuronium (2 mg/kg/h) was delivered intravenously to immobilize the animal.

**Zebrafish preparation.** A 25% w/v solution of Cal520 dextran conjugate (3,000 MW, AAT Bioquest, California) in zebrafish external solution (134 mM NaCl, 2.9 mM KCl, 2.1 mM CaCl₂, 1.2 mM MgCl₂ and 10 mM HEPES glucose, pH 7.8)[53] was pressure injected into the ventral spinal cord of 6-d postfertilization *mitfa*⁻/⁻ (nacre)[37] fish larvae just anterior to the anal pore, following standard procedures[36]. The larvae were left in E3 embryo medium (5 mM NaCl, 0.17 mM KCl, 0.33 mM CaCl₂ and 0.33 mM MgSO₄) at 28 °C overnight to allow retrograde filling of reticulospinal neurons. On the next day before imaging, larvae were paralyzed by bath application of 1 mg/ml of α-bungarotoxin (Molecular Probes) in embryo medium for 1 min. Larvae were mounted dorsal-side up on dishes coated with Sylgard 184 (Dow Corning) in a small drop of 1.5% low melting point agarose (Invitrogen) and covered with embryo medium. During imaging, the dish containing the larval zebrafish was mounted on top of an acrylic platform with an attached speaker that delivered acoustic and mechanical stimuli. The stimulus, which consisted of a 500-Hz sinusoidal waveform lasting 4 ms, was delivered every 100 s. Images were acquired for 5 s before and after the stimulus, which was repeated nine times.

**Fly preparation.** Flies were prepared for two-photon imaging as previously described[39]. Briefly, flies were anesthetized on ice and transferred to a cold plate

at 4 °C. They were glued to a stick with UV glue and inserted into an imaging holder (made from a stainless steel shim using a laser mill) with micromanipulators under a dissection stereomicroscope. The fly's head and a part of the thorax were glued to the holder using UV gel. The holder isolated the back of the fly's head and a small part of the thorax for imaging while leaving the fly's eyes fully exposed for visual stimulation. The cuticle on the backside of the fly's head was removed with dissection needles and forceps and the brain of the fly was exposed for two-photon imaging. To minimize brain movement, we immobilized the fly's proboscis by pressing it into the fly's head and fixing it with wax. We additionally cut muscle M16 or the nerves innervating the muscle. The holder with the fly was then transferred to the microscope for two-photon imaging.

**Visual stimulation for the mouse and the fly.** UV (320–380 nm, peak at 365nm, Richard Wolf) and visible (450–495 nm, peak at 472nm, SugarCUBE) light was used to evoke activity in the fly and the mouse brains, respectively. Visual stimuli were presented by back projection on a screen made of Teflon film (McMaster-Carr) using a custom-modified DLP projector[54]. For mouse experiments, the screen was positioned 17 cm from the right eye, covering $75° × 75°$ degrees of visual space and oriented at ~40° to the long axis of the animal. Full-field square gratings were presented for 12 s (static for the first and last 2.5 s and moving during the middle 7 s) at 12 orientations (0° to 330° at 30° increments) in pseudorandom sequences. A total of ten trials were repeated in each measurement. For some experiments, blank screens with equal mean luminance were presented between grating stimuli. Only data collected during grating movements were used to calculate orientation tuning curves. Gratings had 100% contrast and 0.07 cycles per degree, and they drifted at $26°$ s$^{-1}$ (2-Hz temporal frequency). The same stimulus protocol was used for the fly, except that the body axis of the fly was orthogonal to the screen. During mapping of single-spine calcium transients, gratings with reduced contrast, together with anesthesia, were used to minimize the firing of somatic action potentials[11].

**Image processing, analysis and statistics.** Imaging data were processed with custom programs written in Matlab (Mathworks) or Fiji[55]. Images were registered either with an iterative cross-correlation-based registration algorithm[52], or with the TurboReg plugin in Fiji. ROIs were selected and outlined manually. The averaged fluorescent signal within the ROI was used to calculate calcium transients. A Gaussian filter (size 5 and s.d. = 3) was used to smooth the traces in **Figures 1**, **3** and **4** and in **Supplementary Figures 5**–**7**. For GCaMP6s$^+$ inhibitory neuron experiments (**Fig. 3**), neuropil background was subtracted from averaged signal before calculating calcium transients (**Supplementary Fig. 5**).

For experiments that characterized the tuning of dendritic spines (**Fig. 2**), BAP-induced calcium signal in the spine was removed from the measured transients as described previously[11,12]. Briefly, BAP-induced signal was calculated from a ROI covering the entire dendritic shaft in the image. This global dendritic signal was then removed from the spine signal using a robust regression method (robustfit function in Matlab). The response $R$ of each spine to a visual stimulus was defined as the average $\Delta F/F$ across the 7-s window of drifting gratings.

The distribution of $R$ was assumed to be normal and variances were assumed to be equal across grating angle $\theta$ but this was not formally tested. A spine was defined as orientation-selective if its responses across the various drifting directions were significantly different (ten trials, one-way ANOVA, $P < 0.01$). For these spines, we determined their preferred grating drifting angle $\theta_{pref}$ by fitting their normalized response tuning curves (for example, **Fig. 2d** and **Supplementary Fig. 4d**) with a bimodal Gaussian function[56]:

$$R(\theta) = R_{offset} + R_{pref}e^{-\frac{\text{ang}(\theta - \theta_{pref})^2}{2\sigma^2}} + R_{oppo}e^{-\frac{\text{ang}(\theta - \theta_{pref} + 180)^2}{2\sigma^2}}$$

where $R_{offset}$ is a constant offset, and $R_{pref}$ and $R_{oppo}$ are the responses at $\theta_{pref}$ and $\theta_{pref} - 180°$, respectively. The function $\text{ang}(x) = \min(|x|, |x - 360|, |x + 360|)$ wraps angular values onto the interval 0° to 180°.

For the one-way ANOVA analysis, no statistical methods were used to predetermine our sample sizes (i.e., ten trials for each visual stimulus), but they are similar to those reported in previous publications[52]. Data distribution was assumed to be normal, but this was not formally tested. Data collection and analysis were not performed blind to the conditions of the experiments. No data were excluded from the analyses. A **Supplementary Methods Checklist** is available.

**Code availability.** Matlab codes used for the calculation of phase patterns on the SLM, annular masks/filters, point spread functions of the Bessel foci, as well as for the design of the Bessel module are included in **Supplementary Software**. BesselBeamDesignFlowChart_v2.m provides a step-by-step guide on designing a Bessel module that generates Bessel foci of various NAs and FWHMs for an existing microscope. PSFofBesselBeam_binary.m calculates the two-photon excitation PSF. Calling findPeakAndTrough_v2.m, singleAnnularFilterDesign.m designs annular filters, returns the period of the binary pattern on the SLM, the focal length of L1 and the axial FWHM of generated Bessel foci. patternOnSLMGenerator.m generates binary pattern used for SLM. See **Supplementary Technical Note** for more details on these codes.

**Data availability statement.** The data that support the findings of this study are available from the corresponding author upon reasonable request.

51. Goodman, J.W. *Introduction to Fourier Optics* (Roberts & Company, 2005).
52. Sun, W., Tan, Z., Mensh, B.D. & Ji, N. Thalamus provides layer 4 of primary visual cortex with orientation- and direction-tuned inputs. *Nat. Neurosci.* **19**, 308–315 (2016).
53. Drapeau, P., Ali, D.W., Buss, R.R. & Saint-Amant, L. *In vivo* recording from identifiable neurons of the locomotor network in the developing zebrafish. *J. Neurosci. Methods* **88**, 1–13 (1999).
54. Tan, Z., Sun, W., Chen, T.-W., Kim, D. & Ji, N. Neuronal representation of ultraviolet visual stimuli in mouse primary visual cortex. *Sci. Rep.* **5**, 12597 (2015).
55. Schindelin, J. *et al.* Fiji: an open-source platform for biological-image analysis. *Nat. Methods* **9**, 676–682 (2012).
56. Carandini, M. & Ferster, D. Membrane potential and firing rate in cat primary visual cortex. *J. Neurosci.* **20**, 470–484 (2000).